Synthesis and characterization of Fe-substituting BaO nanoparticles by sol-gel method

N. Abbas[a] , J. M. Zhang[a*], S. Nazir[a] , H. Akhtar[b], M. Zaqa[c], S. Saleem[d], G. Mustafa[e]
[a]*College of Physics and Information Technology, Shaanxi Normal University, Xian, 710119, Shaanxi, P.R China.*
[b]*National Synchrotron Radiation Laboratory, CAS Center for Excellence in Nanoscience, University of Science and Technology, Hefei 230039, P.R China.*
[c]*College of Physical Science and Technology, Yangzhou University, Yangzhou, Jiangsu, China, P.R China*
[d]*Shaanxi Key Laboratory for Advanced Energy Devices and Shaanxi Engineering Lab for Advanced Energy Technology, Xian 710119, P.R. China.*
[e]*Department of Physics, Bahauddin Zakariya University Multan 60800, Pakistan*

Barium oxide have wide attention towards electronic device applications because of their exceptional structural, optical, electrical properties. Sol-gel process was used to prepare the nanocrystalline barium oxide. XRD investigation confirms that that the synthesized Barium oxide nanoparticles highly crystalline nature and have tetragonal structure. The crystal size measured by Scherrer formula and obtained values lies in the range (2.3-6.7nm). The SEM micrographs revealed a reducing agglomeration and porosity with the enrichment in the doping content. IR analysis revealed that prepared samples have high purity while Raman spectra exhibited that the bands intensity of the synthesized nanoparticles was enhanced due to enhancement in force constant with the addition of doping content. UV-vis spectra analysis, performed to study the optical properties, revealed that optical band gap was decrease with increase of the doping content and obtained band gap results lies in the range (1.99-1.85 eV). Moreover, the conductivity of the prepared sample was observed increased from 7.28×10^{-5} Ʊ cm^{-1} to 1.79×10^{-3} Ʊ cm-1, while the resistivity was decreased from 1.1×10^{4} Ω cm to 5.58×10^{2} Ω cm with the increasing of the doping content. The explored results exhibited that the doping iron content, enhanced the characteristics of prepared oxides. Such characteristics of BaO make a potential candidate for electronic device applications.

(Received August 28, 2023; Accepted November 1, 2023)

Keywords: Fe-doped barium oxide nanoparticles, Sol-gel, XRD, FTIR, UV-Vis

1. Introduction

An increased demand for transience has emerged in recent years as electronics become increasingly incorporated into our daily lives. Nanoscience and nanotechnology play a vital role for applied materials research due to their considerable number of applications which depend on its shape and size [1]. The semiconductors are also widely used for optoelectronic related devices such as, solar cells, laser, non-linear optical devices, and photovoltaic devices [2]. Among various semiconductor oxide nanomaterials, barium oxide nanostructures have attained wide attention due to its direct band gap type, group II-VI semiconductor nanomaterial have exceptional importance because of their wide band gap, excellent properties and wide applications such as, electrical energy production, catalysts, self-cleaning devices, and sensors [3,4]. In the past decade, transition metal oxide semiconductors, such as Nickel oxide (NiO), Copper oxide (CuO), Zinc oxide (ZnO), and Barium oxide (BaO), etc are known as the unique semiconductor family because of their

* Corresponding authors: jmzhang@snnu.edu.cn
https://doi.org/10.15251/DJNB.2023.184.1327

increasing study and potential applications. Apart from this, the unique property of BaO is the special interest in the electron field emission, diagnostic imaging, gas sensors, solar energy conversion, catalysts, electronic device and optoelectronic device applications [5,6] due to its major use in the area for electronic devices. In current study, pure BaO and Fe-doped BaO NPs have been used for electronic device applications. The physical properties of the synthesized oxides are normally depending on the particle size, synthesis method, and microstructures such as, surface morphology, crystal defects, grain boundaries, in addition, also depends on doping content [7-9]. Several approaches have been used to prepare metal oxide such as Hydrothermal [10], chemical vapor deposition [11], co-precipitation [12], Sonochemical [13], and sol-gel [14] are examples of a chemical method, while sputter deposition [15] and thermal evaporation [16]. The role of dopants such as transition metals (i.e., Fe, Cu, Co, Ni, and Zn) assist in enhancing electronic, optical, structural and several other properties of the metal oxide. In current work, Fe-doped of Barium oxide NPs have exhibited the electrical, vibrational mode, optical, and structural properties exceptional improvement in unique features, i.e., electrical conductivity, phase purity, and energy band. Barium oxide has lower electrical conductivity as compared to other transition metal oxides which hinder its electrical properties for electronic devices. In order to solve this major problem, the doping of iron (Fe) has been hosted into Barium oxide by sol-gel method. The novelty of this work is the band gap was very low as compared to the actual band gap of the Barium oxide and the electrical resistance was decreased with the enhancement in the dopant content while the electrical conductivity was highly increased, this may be due to the addition of iron (Fe) metal into Barium oxide which enhance the energy carriers. The present activity is supported to the electronic device applications and BaO nanoparticles doped with 4% Fe possess better performance for the electronic device applications. In this communication we have reported the effect of Fe^{+3} substitution (1 % and 4 %) on the physical, optical and electrical properties of mixed Barium oxide.

2. Materials and methods

2.1. Samples preparation and equipment

All chemicals utilized in the experiment are analytic reagent grade. Barium nitrate ($Ba(NO_3)_2$ (Sigma-Aldrich, India, 98%), iron (III) nitrate ($Fe(NO_3)_3\ 9H_2O$, citric acid (CA) and ammonia (NH_3) solution. An aqueous solution of Barium nitrate, citric acid and iron (III) nitrate were prepared into 100 ml deionized water. The chemical solution kept on continuous heating of magnetic stirrer at 100ºC for 6 h. The ammonia solution was added drop by drop to this chemical solution to maintain pH 7. After a few hours, the chemical solution changed into transparent sol which on further heating changed into dry gel that was changed into powder after combustion on the further continuous heating. The prepared powder was fully grinded. The prepared powder was put into furnace to enhance crystallinity. The obtained final product was Barium oxide nanoparticles. Moreover, two samples Fe-doped (with the addition of 1 % and 4 %) Barium oxide nanoparticles synthesis following the similar procedure. The X-ray diffraction (XRD) patterns were obtained at room temperature by powder samples in an X-ray diffractometer (MSAL-XD2, Cu-Kα) to study the structural parameters. The surface morphology and microstructure of the samples were studied by scanning electron microscope (SEM) (HITACHI S-520). FT-IR spectrum was recorded using Perkin-Elmer infrared spectrometer Model C-783 in the range 500-4000 cm^{-1}. In addition, Raman spectroscopy for the Raman active mode. UV–visible absorption spectra were recorded using a UV-Vis-Perkin Lambda 25 spectrometer and the I-V characteristic curve investigation was performed by a Keithley Electrometer to study the electrical properties. For examine the I-V characteristics, pellets of 2.5 mm width were developed by engaging the 3 tons' pressure into a hydraulic press machine.

2.2. Calculations

The different structural parameters such as lattice constant, unit cell volume, X-ray density bulk density, porosity, micro strain, dislocation density and average crystallite size (D) nm was

determined by using the Scherer's equations. All the parameters by using X-ray diffraction data were calculated using the following formula [17-21].

$$\frac{1}{d^2} = \left(\frac{h^2+k^2}{a^2}\right) + \frac{l^2}{c^2} \quad (1)$$

$$V_{cell} = a^2 c \quad (2)$$

$$\rho_{X\text{-}ray} = \frac{Z\,M}{N_A\,V} \quad (3)$$

$$\rho_B = \frac{m}{V} \quad (4)$$

$$P\,\% = \left(1 - \frac{\rho B}{\rho x}\right) \quad (5)$$

$$\delta = \frac{1}{D^2} \quad (6)$$

$$\varepsilon = \frac{(\beta \cot\theta)}{4} \quad (7)$$

$$\beta_{hkl} \cos\theta = \frac{0.9\lambda}{D} + 4\varepsilon \sin\theta \quad (8)$$

$$D = \frac{k\,\lambda}{B_{(hkl)}\cos\theta} \quad (9)$$

where β_{hkl} is the full width at half maximum (FWHM) of the diffraction peak, 'λ' is the X-ray wavelength, 'k is the Scherrer constant whose value is 0.94, and 'θ' is the diffraction angle. 'Z' is the constant reliant on the crystal structure of the synthesized specimen and is equal to the number of the lattice points per unit cell, in current study, the material has cubic crystal structure whose atomic number value is '8', 'M' is known as molecular weight, (a^3) is unit cell constant and N_A is Avogadro's number.

3. Results and discussions

3.1. Crystal structure analysis

Phase and crystallinity of as-synthesized pure sample and Fe-doped BaO Barium oxide nanoparticles were conducted by the XRD with CuKα radiations (λ=.5406 Aº) in the 2θ range of 15-65º. Fig. 1 shows the diffraction peaks at 19.65º, 24.32º, 26.91º, 33.61º, 42.24º, 43.03º, 44.84º 55.97º and 60.95º are assigned to (120), (101), (110), (112), (103), (211), (114) and (222) planes, respectively. All the peaks of three samples are well matched with the JCPDS card No. 89-8425, which has tetragonal structure. The observed patterns are also confirmed with the reported literature [22-24]. The represented Sample A (pure BaO), Sample B (1% addition of iron $Fe_{0.01}$ $Ba_{0.09}O$) while Sample C (4% addition of iron $Fe_{0.04}$ $Ba_{0.96}O$) have been carried out by the Sol-gel method respectively. The intense and sharp peaks show that the prepared nanoparticles have a high crystalline nature. The effect of addition of iron observed, the intensity of diffraction peaks, increased that attributed to the enhancements in the growth of crystal which affirmed the synthesis metal oxides have crystallinity nature while the symmetry and crystal structure remains same as shown in Fig.1.

It is also attributed that the incorporation of different ionic radius of dopant Fe^{2+} (0.78 Å) forms an interstitial substitution in the host Ba^{2+} (1.35 Å) lattice locations [25, 26]. The crystallite size was determined by Scherer's formula, and obtained values lies in the range (2.3-6.7 nm). The Sample C have higher crystallite size as compared to Sample A and Sample B. The reason of increasing crystallite size, it may be more minor ionic radii of dopant as compared to that of parent Ba^{2+}, it will form the shrinking impact in strain on the lattice sites of BaO. The other factors to increase the crystallite size, due to some behind mechanisms. Firstly, because dopants' lower

affinity for interacting with O^{2-} may promote the formation of heterogeneous nucleation spots in the reaction media. It consequently continues to grow close to the BaO lattice. Secondly, the energy of grain boundaries through its interaction with surface boundaries or surface energy may be affected by the presence of dopant which may lead to the formation of more surface boundaries [27]. In other words, the lattice strain might be decreased by minor ionic radii dopants and conversely enhanced the crystallite size [28].

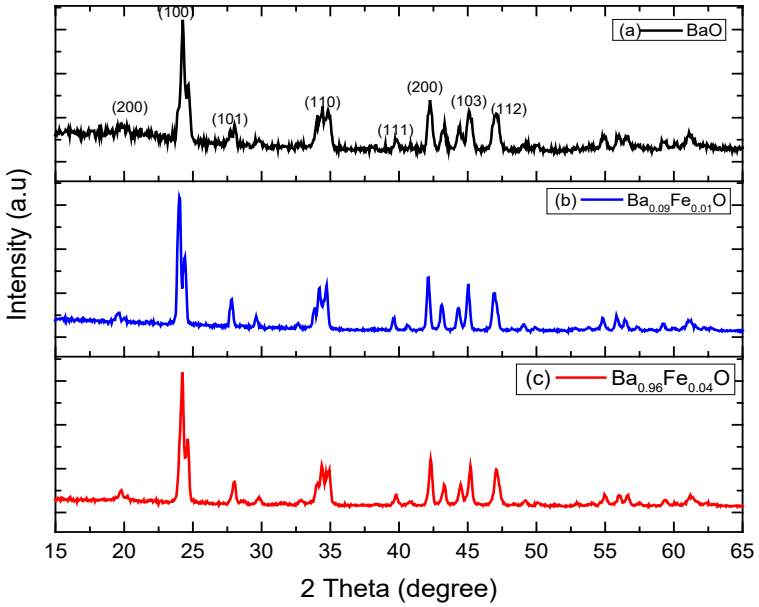

Fig.1. X-ray diffraction patterns of (a) pure BaO, (b) $Fe_{0.01}Ba_{0.09}O$, and (c) $Fe_{0.04}Ba_{0.96}O$ samples.

It is observed that the lattice constant and unit cell volume were decreased due to the addition of dopant content which obey the Vergard's law. The reason is that the larger ionic radii of parent Ba^{2+} (0.73 Å) may be replaced with smaller ionic radii of (1.31 Å). X-ray density was measured by Eq.3 and obtained values lies in the range (6.1-4.9 g/cm^3) the reduction in X-ray density is related to the fact that the lattice volume decreases with the increasing of Fe-content [29]. The bulk density is determined using Eq.4. It has been noted that bulk density was decreased from (5.5-4.7 g/cm^3) with the enhancement in the iron metal doping content from pure Sample A to Sample C.

In a microstructure, porosity is the presence of microscopic voids within a material, either between the grains or trapped within them. Materials with pores can absorb liquid or moisture, which leads to corrosion. Porosity was calculated by Eq 5. The calculated values show that porosity decreases with the increase in doping content. Porosity in any material gives information about its morphology and optical properties. The sample doped with 4 % iron doping content exhibited least porosity 3.1 %. The presence of porosity in the microstructures can be seen from the SEM micrographs in Fig.5. The observations revealed that the synthesized material shows a highly crystalline nature and become a potential candidate for the electronic devices.

It is determined from the square of reciprocal of crystallite size which is given in Eq.6. The dislocations are the imperfections in crystals that result from lattice mismatches between different crystallographic regions. In current study, the number of dislocations decreases with the substitution of doping ion into parent crystal system of BaO. It means that the addition of dopant ions causes to reduce the crystal imperfections or lattice defects which confirmed that Sample A pure BaO at Sample-C revealed the better crystallinity. The decrease in number of dislocations may be attributed to the decrease in FWHM and increase in peak intensity enhance the crystallite size; consequently, the decline in dislocation density occurs with 4 % addition of Fe dopant into BaO crystal system. The reduction in dislocations may be due to the movement of Fe ions from

crystallite to grain boundary. It can be concluded from the above discussion that BaO nanoparticle at 4 % Fe substitution content shows better crystallinity. The microstrain of the prepared samples are calculated using Eq 7. Atomic variations from the reference lattice position during the formation of nanoparticles lead to stress, which causes the microstrain [30]. Moreover, the Sherrer's relation only gives data about the average crystallite size, but it ignores the consequences of the microstrain in BaO, $Fe_{0.01}BaO$, $Fe_{0.04}BaO$ NPs. Hence, the William-Hall equation is used to calculate the microstrain and crystallite size of each samples [31]. Plotting $\beta_{hkl}\cos\theta$ versus $4\sin\theta$ (Fig.2) using the William-Hall term results in a straight line, with the intercept ($0.9/D_{WH}$) representing the crystalline size and the slope (ε) representing the microstrain [32]. Different crystalline sizes were observed in the computed values from the Scherrer's and William-Hall methods, dislocation densities and microstrain of pure BaO, $Fe_{0.01}Ba_{1-0.01}O$, $Fe_{0.04}Ba_{1-0.04}O$ NPs.

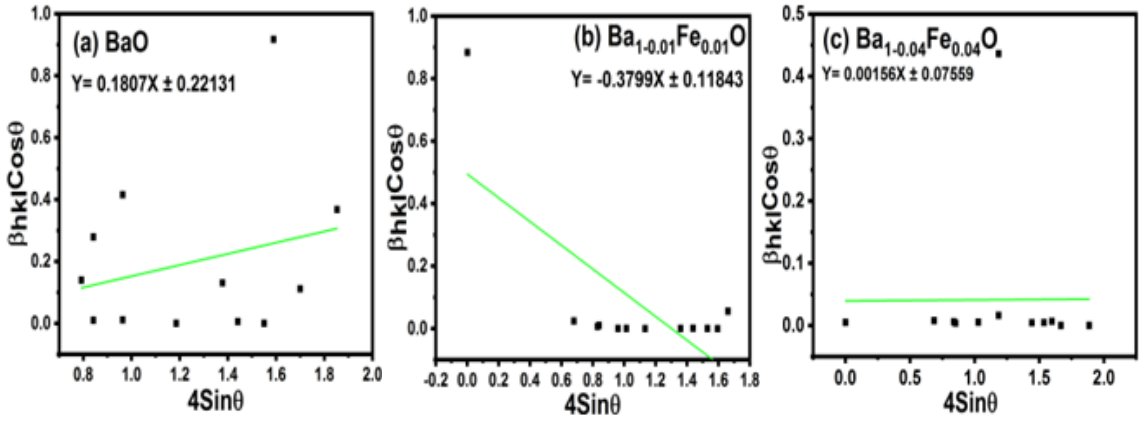

Fig. 2. W-H plot of (a) pure BaO, (b) $Fe_{0.01}Ba_{0.09}O$, and (c) $Fe_{0.04}Ba_{0.96}O$ samples.

The inclusion of strain in the synthesized samples is mostly responsible for the variance in crystalline size, and their calculated strain values are acceptable. The observation shows that the microstrain is inversely associated to the crystalline size i.e., the crystalline size of synthesized samples with the addition of doping content increases with the increase of the microstrain and vice versa. From these analyzed different structural parameters, it can be concluded that Fe metal doping improves the structural properties of BaO NPs by enhancing the reducing crystallographic defects and microstrain, and increasing crystallinity of that material.

3.2. FTIR spectra studies

The IR characterization tool provides information about the positions of functional groups molecules, crystals, crystal vibration modes, and interaction of molecules [33]. The most effective technique which identifies the possible functional groups involved in the as-synthesized BaO samples. Fig.3 shows, FTIR spectra of Fe-doped Barium oxide samples were recorded in the range of 500-4000 cm^{-1} at the room temperature.

IR spectrum exhibited the strong band found in the range of 670-720 cm^{-1} correspond to the Ba-O bond formation. The Ba-O stretching vibration is exhibited by a weaker absorption band obtained in the range 610-650 cm^{-1}. The O-H stretching vibration mode observed in the range 1730-1780 cm^{-1}. The peak between 1380 cm^{-1} and 1440 cm^{-1} may be caused by the creation of barium carbonate, which is due to BaO NPs absorbing ambient CO_2. The O-O stretching modes vibration found between ~1030-1090 cm^{-1} [34]. The peak found between 840-880 cm^{-1} related with the asymmetric vibration mode of NO_3^{-1} ions [35]. The obtained similar results reported in the literatures [36,37].

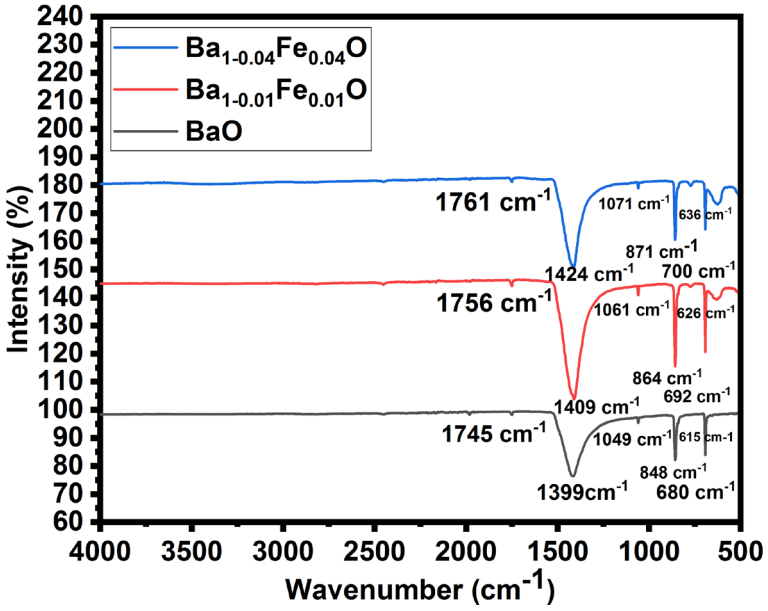

Fig. 3. IR spectra of (a) pure BaO, (b) $Fe_{0.01}Ba_{0.09}O$, and (c) ${}_6Fe_{0.04}Ba_{0.9}O$ samples.

3.3. Raman analysis

Raman spectra for all synthesized, Fe-doped BaO samples are shown in Fig.4. It is evident from the graph that the peaks of pure BaO and Fe-doped BaO samples have nearly the same positions. The most significant mode of vibration in BaO powder is connected to the peaks at 398 cm^{-1}, 427 cm^{-1}, and 443 cm^{-1} respectively. The Raman spectra showed an increase in its intensity and a red shift to 398 cm^{-1}, 427 cm^{-1}, and 443 cm^{-1}, which revealed structural alterations because of the mechanical activation. The strong peaks observed at 759 cm^{-1}, 769 cm^{-1}, 777 cm^{-1} in the graph which confirmed the perfect substitution of Fe content.

In this work, the absence of any additional peaks reveals the purity of the prepared specimens. Moreover, it is also noted that the peaks intensity of all the samples increases which confirmed the crystallinity. The volume expansion occurred in the BaO NPs due to the doping of 1 % Fe, consequently the force constantly decreases because of the rising inter-atomic distances. While the doping of 4 % Fe causes the further volume expansion in the BaO NPs, as a result the force constant decreases because of the further increasing inter-atomic distances, this factor increases the bands intensity of the BaO nanoparticles.

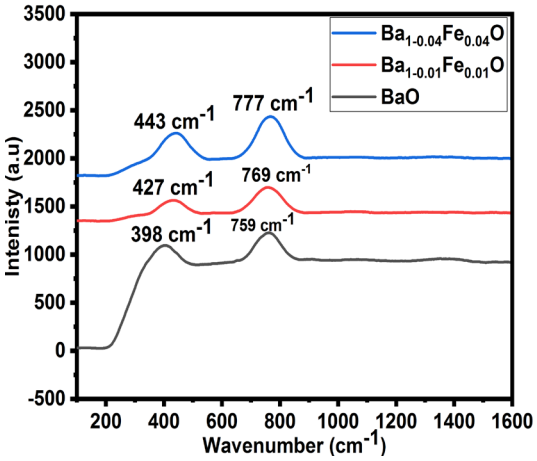

Fig. 4. Raman spectra of (a) pure BaO, (b) $Fe_{0.01}Ba_{0.09}O$, and (c) $Fe_{0.04}Ba_{0.96}O$ samples.

The variation in wavenumber during vibration transitions is proportional to $K^{1/2}$, where K is referred to as the force constant. the higher force constant becomes a cause to shift the Raman bands to a high wavenumber. Secondly, materials shape and grain size of NPs play vital role. Hence, the synthesis samples shown strong intensity and sharp band spectra with higher intensity.

3.4. Morphology analysis

Fig.5 shows the micrograph of the synthesized BaO, $Fe_{0.01}Ba_{0.09}O$, $Fe_{0.04}Ba_{0.96}O$ samples while Fig.6 shows the histograms of the respective micrographs, and also determined grain size by imagej sotware. The obtained average grain size lies in the range of 3.4-5.2 μm. Fig.5 it is cleared that, images of the composed material is different such as agglomerated flower like shape, porous shape, and cloud like shape, respectivelly. It is concluded from the Fig.5 grain boundries were not clear and showed non uniform distribution of the particles, but with the addition of Fe doping element grain boundries slightly become clear. BaO nanoparticles doped with 4 % Fe ions showed more clear boundries as compared to pure BaO and 1 % Fe doped BaO. It is observed from the Fig.5 that, in the case of pure BaO sample agglomeration is maxium and then gradually decreases with increase in doping content of Fe minimum agglomeration is seen at 4 % Fe doped BaO. Agglomiration decreases gradually with the enhancement in doping content, this is because of the reduction in force of attraction among atoms as a result particle size increases. Therefore BaO doped with 4 % of Fe,shows higher particle size of 5.2 μm. This increasing prticle size also reduces the energy band gap between the valence and conduction bands, which in turn, makes the electrons to conduct between valence and conduction bands. In other wors, it can be said that the doping effect reduces the agglomeration among particles, which in turn, improves the optical and electrical characteristics with morphotology. It has found that the porosity of the material gradually reduces, with enhancement in dopant content as BaO doped with 4% Fe showed lower porosity. The reduction poroisty means enhances the physical properties of BaO nanoparciles.

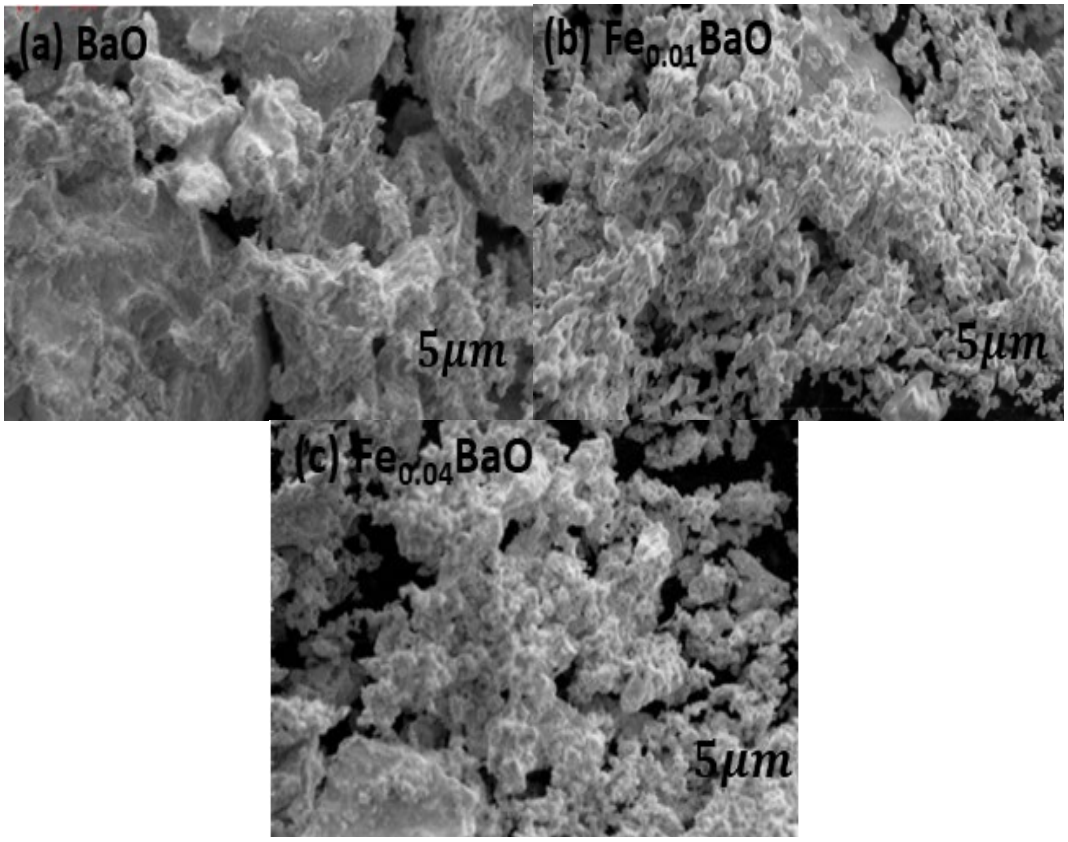

Fig. 5. SEM micrographs of (a) pure BaO, (b) $Fe_{0.01}Ba_{0.09}O$, and (c) $Fe_{0.04}Ba_{0.96}O$ samples.

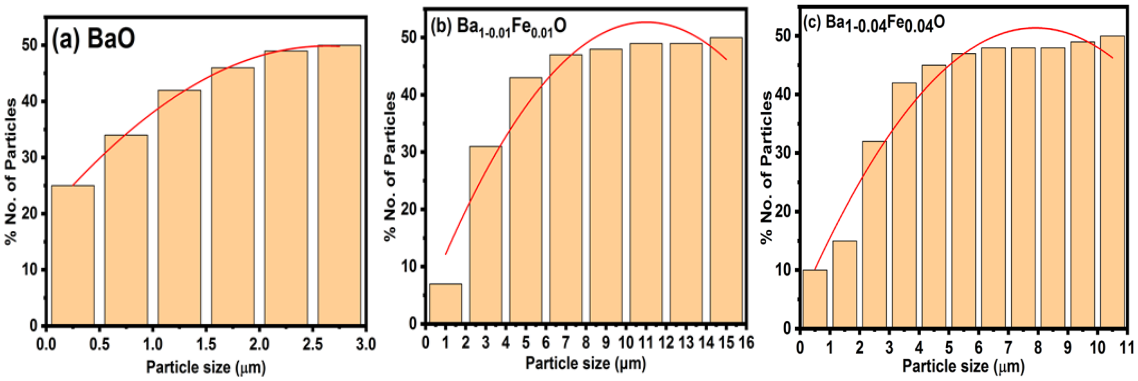

Fig. 6. Histograms of the (a) pure BaO, (b) $Fe_{0.01}Ba_{0.09}O$, and (c) $Fe_{0.04}Ba_{0.96}O$ samples.

3.5. Optical properties

The optical properties including the optical band gap and electronic transitions of produced BaO nanoparticles were determined by analyzing with the optical absorption spectrum. The photons having energy more than band gap of semiconductor are absorbed by this semiconductor, consequently, the electrons transmit from the valence band to the conduction band. Consequently, there is rise in wavelength absorbency of the material corresponding to the band gap energy. The kind of electronic transitions determines how the absorption relates to the incident photon energy; if momentum is conserved, the transition is direct; otherwise, it is indirect [38].

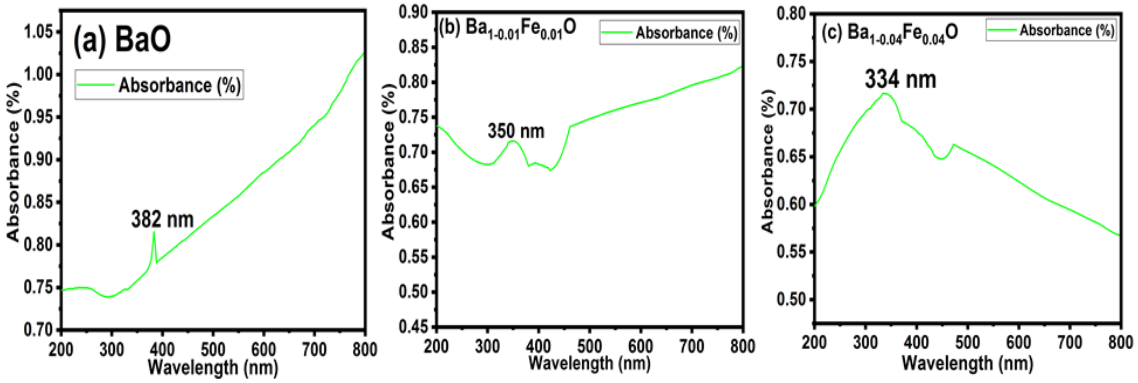

Fig. 7. UV-Vis absorption spectra of (a) pure BaO, (b) $Fe_{0.01}Ba_{0.09}O$, and (c) $Fe_{0.04}Ba_{0.96}O$ samples.

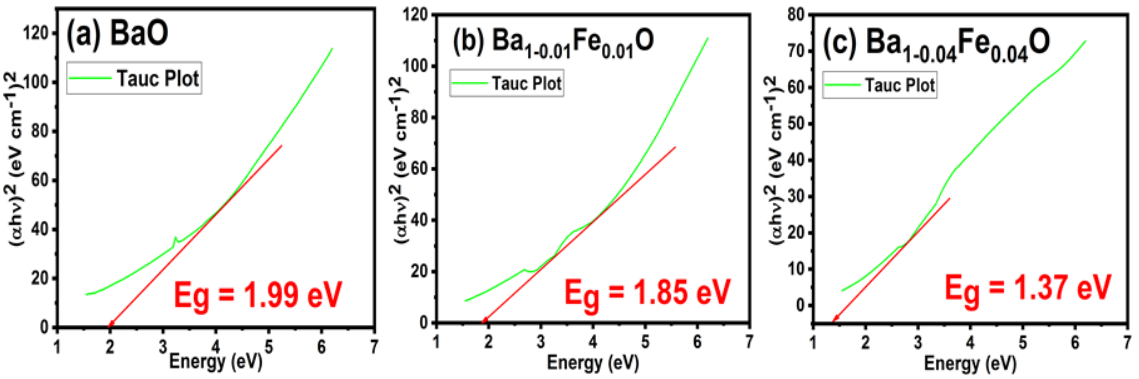

Fig. 8. Tauc plot for band gap of (a) pure BaO, (b) $Fe_{0.01}Ba_{0.09}O$, and (c) $Fe_{0.04}Ba_{0.96}O$ samples.

The absorption spectra of produced specimens are given in Fig.7. Maximum absorption is seen in the UV band between 300 and 400 nm as a result of the charge transfer between the O^{2-} 2p and Ba 4f states. According to the spectral profile, the charge transfer transition of Ba^{2+} and the $4f^{l}$ $5d^{1}$ of Ba^{1+} transition overlap. There is no absorption was seen above the wavelength of 500 nm. With increasing iron (Fe) dopant content, which is connected to BaO powder data, the absorption edge can be seen to shift toward shorter wavelengths (blue-shift) in the spectra. Fig.8 shows the Tauc plot of pure and Fe-doped BaO NPs samples was determined by this relation:

$$\alpha h\nu = B\,(h\nu - Eg)^{1/2} \tag{10}$$

where 'E_g' is the direct band gap, 'α' is the optical absorption coefficient, 'B' is a constant, and 'hν' is the photon energy [39]. The obtained band gaps are 1.99 eV, 1.85 eV, and 1.37 eV, respectively. Fig.8 exhibits that the rise in dopant content outcomes in the decrease of band gap. In the case of the 4% Fe-doped BaO nanoparticles, band gap has lowest value. This decline of band gap energy with the addition of dopant content may be due to a reason that this doping element forms the localized states that are nearer to the conduction band, so the band gap falls. Fe ion doping results in the production of interstitial sites, which in turn creates new energy states between the valence and conduction bands, explaining why performance is improved in the case of 4%-doped BaO nanoparticles. Under the visible light area, the impurity energy levels enable intrinsic band gap excitation. This shows that the conduction band of BaO can be stimulated to the high state of 3d-electrons from Fe-cation dopants, so improving its electronic performance. Another reason is that the lower band gap is due to the lower energy of conduction band minimum. The similar results are reported in the literature [40]. Moreover, the obtained band gap revealed that the BaO semiconductor has electronic properties in the range of conventional semiconductors. The narrow band gap gives the ability to electronic devices to operate at lower temperatures.

3.6. Electrical measurement

The electrical characteristics of the synthesized samples shows semiconductor behavior. At room temperature, I-V curves of the synthesized samples with potential ranges of -20 to 20 V were measured. It is observed that the graphs exhibited a high current value for the terminal voltages. The Eq.11 was used to determine the electric current flow from the circuit:

$$N = \frac{Q}{K_B\ T}\ x\ \frac{d_V}{d\ I_n\ I_s} \tag{11}$$

where K_B is the Boltzmann constant, Q is the electric charge, T is the absolute temperature, Is is the saturation current, and V is voltage. In the present work, the linear curves of all synthesized samples confirm the ohmic quality (α=1) while α >1 in the case of non-ohmic nature material as per relation:

$$I\ \alpha\ V^{\alpha} \tag{12}$$

The following relation was determining the electrical conductivity of the synthesized samples, while the reciprocal (1/σ) of this relation gives the resistivity of that material [41]:

$$\sigma = \frac{IxL}{VxA} \tag{13}$$

where V is denoted by applied voltage, I is current, 'A' represent cross-sectional area of the pellets, L is the thickness of the pellets. The calculated values of the conductivities of the synthesized samples lies in the range 7.3×10^{-5} to 1.8×10^{-3} Ʊ cm^{-1}, while electrical resistivity was observed 1.1×10^{4} to 5.6×10^{2} Ω cm, Application of the material base on, ohmic nature, in this way, the prepared samples act as a potential candidate for electronic devices. Moreover, the electrical conductivity can be explained on the basis of band gap and charge carriers. In the present work, it is observed that band gap decreases as concentration of dopant increased while conductions between valence and conduction bands of the semiconductor NPs increase and

resistivity decreases. Few factors which increase the electrical conductivity of the nanoparticles by the insertion of Fe ions [42]. In this way, a large amount of electric current is produced in the circuit, consequently, the material becomes a best candidate for electronic device applications.

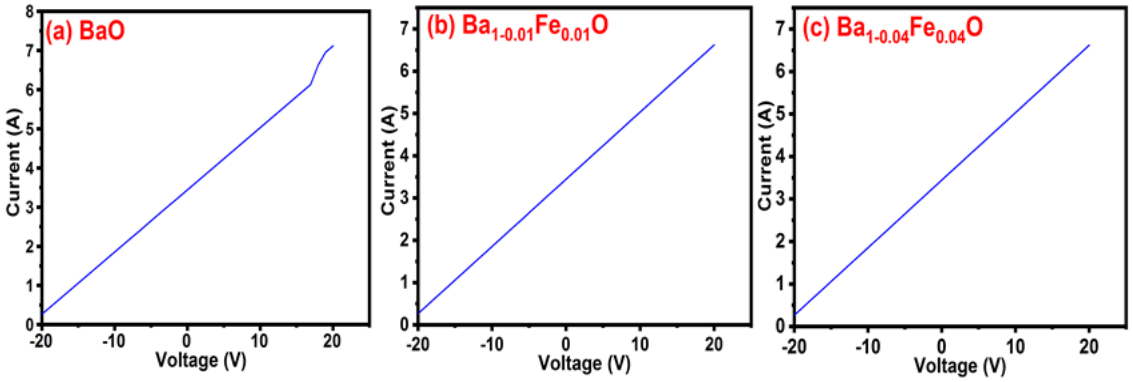

Fig. 9. I-V curves of (a) pure BaO, (b) $Fe_{0.01}Ba_{0.09}O$, and (c) $Fe_{0.04}Ba_{0.96}O$ samples.

4. Conclusions

In this study, Fe-doped BaO nanoparticles were prepared by sol-gel method and analyzed the impact of Fe doping on the structural, morphology vibrational mode, optical, and electrical characteristics of BaO NPs for electronic device applications. The structural properties analysis by XRD and observed tetragonal crystalline structure. The crystal size measured by Scherrer formula and obtained values lies in the range (2.3-6.7nm) while lattice parameters, unit cell volume, porosity exhibit decreasing behavior. The dislocation density which indicates the lattice defects was decreased due to increasing doping content. SEM micrographs reveal that agglomeration and porosity decrease with the increase in the Fe content. IR spectra revealed that the absorption band, purity of the prepared samples and the perfect incorporation of Fe ions in the BaO NPs. Raman spectra exhibited that the intensity of bands is improved with the increase in the force constant which also reveals the high crystallinity of the samples. Band gap was found in the range of 1.99 e V to 1.85 eV by Tauc plot and observed band gap decrease with the increase in the Fe content. The conductivity in the synthesized samples was observed increased from 7.28×10^{-5} ℧ cm^{-1} to 1.79×10^{-3} ℧ cm^{-1} while resistivity decreased from 1.1×10^{4} Ω cm to 5.58×10^{2} Ω cm^{-1} with the increasing doping content. Such characteristics of these materials may be suitable for potential applications such as electronic devices applications

Acknowledgements

The authors would like to acknowledge the Fundamental Research Funds for the Central Universities for providing financial support for this research.

References

[1] V. R. Feig, H Tran, & Z. Bao, ACS central science, 4(3), 337-348 (2018); https://doi.org/10.1021/acscentsci.7b00595

[2] I. Matsui, Journal of chemical engineering of Japan, 38(8), 535-546 (2005); https://doi.org/10.1252/jcej.38.535

[3] Y. Cui, J. Chen, Y. Zhang, X. Zhang, W. Lei, Y. Di, Z. Zhang, Applied Surface Science, 396, 1108-1112 (2017); https://doi.org/10.1016/j.apsusc.2016.11.095

[4] L. Yang, Y.M. Choi, W. Qin, H. Chen, K. Blinn, M. Liu, P. Liu, J. Bai, T.A. Tyson, M. Liu, Nature communications, 2(1), 1-9 (2011); https://doi.org/10.1038/ncomms1359

[5] S. Alarifi, D. Ali, W. Al-Bishri, International journal of nanomedicine, 11, 249 (2016); https://doi.org/10.2217/nnm.15.199

[6] E. Sundharam, A. Jeevaraj, C. Chinnusamy J. of Bionanoscience, 11(4), 310-314 (2017); https://doi.org/10.1166/jbns.2017.1449

[7] R. Renukadevi, R. Sundaram, K. Kasinathan, Journal of Nanostructures, 10(1), 167-176 (2020).

[8] E. Cordoncillo, T.R. Machado, L. Ferrazza, D. Juanes, Progress in Cultural Heritage Preservation. Euro-Mediterranean Conference. Berlin, Heidelberg: Springer; pp. 801-8 (2012); https://doi.org/10.1007/978-3-642-34234-9_85

[9] N. Ahmad, R. Wahab, M. Alam, Journal of Nanoscience and Nanotechnology, 14(7), 5342-5346 (2014); https://doi.org/10.1166/jnn.2014.8852

[10] S.P. Prabhavathi, J. Punitha, P.S. Rajam, R. Ranjith, G. Suresh, N. Mala, D. Maruthamuthu, J Chem Pharm Res, 6, 1472-1478 (2014).

[11] G. Suresh, P.N. Nirmala, Turkish Journal of Physics, 36(3), 392-397 (2012).

[12] R. Renukadevi, R. Sundaram, K. Kasinathan, Journal of Nanostructures, 10(1), 167-176 (2020).

[13] H.R. Momenian, S. Gholamrezaei, M. Salavati-Niasari, B. Pedram, F. Mozaffar, D. Ghanbari, J. of Cluster Science, 24(4), 1031-1042 (2013); https://doi.org/10.1007/s10876-013-0595-y

[14] M. Mabrouk, G. Ibrahim Fouad, H.H. Beherei, D.B. Das - Pharmaceutics, 14(8), 1582 (2022); https://doi.org/10.3390/pharmaceutics14081582

[15] C. Wu, K. Kruska, M.R. Castell - Surface science, 618, 94-100 (2013); https://doi.org/10.1016/j.susc.2013.08.019

[16] Z. Li, Doctoral dissertation, University of Akron (2013).

[17] M. Azim, M.A. Chaudhry, N. Amin, M.I. Arshad, M.U. Islam, S. Nosheen, M. Ahmad, H. Anwar, Digest J Nanomaterial Bio structures 11 (2016).

[18] N. Amin, M.I. Arshad, M.U. Islam, A. Ali K. Mahmood,G. Murtaza, M. Ahamad, G. Mustafa, Digest Journal of Nanomaterials and Biostructures 11(2), 579 (2016).

[19] H. Anwar, Y. Jamil, G. Mustafa, M.U. Islam, A. Shakoor, M. I. Arshad, H. Akhtar, and M. R. S. Aleem, Journal of Ovonic Research Vol 13, no. 5 :241-248 (2017).

[20]. G. Mustafa, M.U. Islam, W. Zhang, Y. Jamil, M. A. Iqbal, M. Hussain, M. Ahmad, Journal of Magnetism and Magnetic Materials, 378, 409-416 (2015); https://doi.org/10.1016/j.jmmm.2014.11.057

[21] G. Mustafa, M.U. Islam, W. Zhang, A.W. Anwar, Y. Jamil, G. Murtaza, M. Ahmad, Journal of Magnetism and Magnetic Materials, 387, 147-154 (2015); https://doi.org/10.1016/j.jmmm.2015.03.091

[22] N. Ahmad, R. Wahab, M. Alam, Journal of Nanoscience and Nanotechnology, 14(7), 5342-5346 (2014); https://doi.org/10.1166/jnn.2014.8852

[23] G. Suresh, P.N. Nirmala, Turkish Journal of Physics, 36(3), 392-397 (2012).

[24] Y. Masubuchi, S. Miyazaki, P. Song, T .Yamamoto, k. Nakano, k. Hongo, R. Maezono, Journal of Alloys and Compounds, 918, 165632 (2022); https://doi.org/10.1016/j.jallcom.2022.165632

[25] Y. Watanabe, Y. Hiruma, H. Nagata, T. Takenaka, Ceramics International, 34(4), 761-764 (2008); https://doi.org/10.1016/j.ceramint.2007.09.023

[26] E. Uchida, M. Murasugi, S. Okuda Minerals, 10(8), 696 (2020); https://doi.org/10.3390/min10080696

[28] V. Boiko, Z. Dai, M. Markowska, C. Leonelli, C. Mortalò, F. Armetta, F. Ursi, G. Nasillo, Scientific reports, 11(1), 1-14 (2021); https://doi.org/10.1038/s41598-020-80335-9

[29] O. Mondal, M .Pal, R. Singh, D. Sen, S. Mazumder, . Journal of Applied Crystallography, 48(3), 836-843 (2015); https://doi.org/10.1107/S1600576715006664

[30] P.S. Aghav, V.N. Dhage, M.L. Mane, D.R. Shengule, R. G. Dorik, K. M. Jadhav, Physica B: Condensed Matter, 406(23), 4350-4354 (2011); https://doi.org/10.1016/j.physb.2011.08.066

[31] G.E. Amidon, P.J. Secreast, D. Mudie, Developing Solid Oral Dosage Forms, 271-293 (2009).

[31] R.S. Kate, S.C. Bulakhe, R.J. Deokate, Optical and Quantum Electronics, 51(10), 1-19.(2019); https://doi.org/10.1007/s11082-019-2026-2

[32] R.O. Yathisha, Y.A. Nayaka, P. Manjunatha, H. T Purushothama, M. M. Vinay, K.V. Basavarajappa, Physica E: Low-dimensional Systems and Nanostructures, 108, 257-268 (2019); https://doi.org/10.1016/j.physe.2018.12.021

[33] S. Ramya, R. Gobi, N. Shanmugam, G. Viruthagiri, N. Kannadasan, Journal of Materials Science: Materials in Electronics, 27(1), 40-48 (2016); https://doi.org/10.1007/s10854-015-3714-8

[34] M. Shoaib, M.Y. Naz, S. Shukrullah, M.A. Munir, A. Ghaffar, M. Irfan, S.N.F Mursal, K. Kamran, Applied Physics A, 128(11), 1-11 (2022); https://doi.org/10.1007/s00339-022-06123-6

[35] S. Abramowitz, N. Acquista, Journal of Research of the National Bureau of Standards. Section A Physics and Chemistry, 75(1), 23 (1971); https://doi.org/10.6028/jres.075A.003

[36] E. Sundharam, A. Jeevaraj, C. Chinnusamy, Journal of Bionanoscience, 11(4), 310-314 (2017); https://doi.org/10.1166/jbns.2017.1449

[37] N. Ahmad, R. Wahab, M. Alam, Journal of Nanoscience and Nanotechnology, 14(7), 5342-5346 (2014); https://doi.org/10.1166/jnn.2014.8852

[38] M.A. Ansari, N.Jahan, Materials Highlights, 2(1-2), 23-28 (2021); https://doi.org/10.2991/mathi.k.210226.001

[39] G. Varughese, V. Rini, S.P. Suraj, K.T. Usha, Advances in materials science, 14(4), 49 (2014); https://doi.org/10.2478/adms-2014-0021

[40] A.A. Ansari, J. Labis, M. Alam, S.M. Ramay, N. Ahmad, A. Mahmood Phase Transitions, 89(3), 261-272 (2016); https://doi.org/10.1080/01411594.2015.1116532

[41] S. Manzoor, S.V. Trukhanov, M.N. Ansari, M. Abdullah, A. Alruwaili, A.V. Trukhanov. T. A. Taha,Nanomaterials, Nanomaterials, 12(13), 2209 (2022); https://doi.org/10.3390/nano12132209

[42] L. Yang, Y.M. Choi, W. Qin, H. Chen, K. Blinn, M.Liu, P.Liu, J. Bai, T.A. Tyson, M. LiuNature communications, 2(1), 357 (2011); https://doi.org/10.1038/ncomms1359